

Mechanism and Constitutive Model of a Continuum Robot for Head and Neck Cancer Radiotherapy.

Olalekan Ogunmolu[†], Xinmin Liu^{*}, Nicholas Gans[‡], and Rodney Wiersma^{*}

Abstract—We present a parallel soft robot mechanism and the constitutive laws that govern the deformation of its constituent actuators. Our ultimate goal is the real-time motion-correction of a patient’s deviation from target pose in frameless and maskless head and neck cancer radiation therapy. The soft actuators control the position of the patient’s cranial region on a treatment machine. In this work, we describe the mechanism, derive the stress-strain constitutive laws under the isochoric deformation principle for the actuators, and then present results that validate our hypothesis. Our simulation results demonstrate deformations consistent with the isochoric volume preservation principle and radially symmetric displacement characteristics.

I. INTRODUCTION

Along with chemotherapy and surgery, radiation therapy (RT) is an effective cancer treatment modality, with more than half of all cancer patients managed by RT having higher survival rates [1]. This is in part due to the technological advancements that enable maximizing radiation dose to a tumor target, whilst simultaneously minimizing radiation to surrounding healthy tissues within a target volume. To assure optimal dose delivery in RT, it is important for the patient to remain in a stable pose on the treatment machine during treatment. The current clinical convention is to immobilize the patient with rigid metallic frames and masks in a process called frame- and mask-based immobilization (see Fig. 1). However, these immobilization mechanisms attenuate the radiation dose (lowering treatment quality), lack real-time motion compensation (hence the need for stopping the treatment when the patient deviates from a target position beyond a given threshold), and they cause patient discomfort and pain [2].

Systems such as the Cyberknife (see right inset of Fig. 1), though ensuring complete non-invasive radiotherapy, are incapable of closed-loop, real-time head motion correction when the treatment beam is on. This is because they are only capable of compensating motion based on pre-calculated trajectories. Furthermore, they have limited effectiveness given their non-compliant parts that assume rigidity of the patient’s body.

Techniques employed for immobilization up until now in clinics range from open-loop motion compensation systems (where the whole treatment is stopped whenever the patient deviates from target), to robot-based closed-loop systems.



Fig. 1: *Left Inset:* Mask/Frame Immobilization in Frame-based RT. *Right Inset:* The Cyberknife and 6-DOF robotic couch system. ©Accuray Inc. [Image best visualized in colored print].

Initial frameless and maskless (F&M) RT research consisted of semi-rigid and soft devices around the patient’s head and neck (H&N) region without a closed-loop feedback controller. These techniques were mostly evaluative studies meant to investigate the feasibility of non-rigid immobilization techniques in treatment planning [3]–[8], often achieving a higher real-time positioning accuracy. Utilizing rigid parallel robots, they provide better positioning accuracy owing to their inherent defenses against the large flexure torques and error magnification of open kinematic chains. With rigid electro-mechanical links connected at discrete joints, they correct motions in controlled settings. Example implementations include the steel-cast 4-DOF assembled robot of [9], the HexaPOD of [10], or the fabricated Stewart-Gough platform of [11]. However, these systems are accompanied by the following hazards:

- they share their dexterous workspace with the patients’ body – a safety concern since these robots’ rigid mechanical components exhibit almost no compliance;
- their lack of structural compliance mean that the patient experiences “hard shocks” when the end effector moves; and
- they are incapable of providing sophisticated motion compensation that may be needed for respiratory and internal organs displacement that often cause deviation from target.

Furthermore, the attenuation of the ionizing radiation owing to interference with the mechanical robot components is often left unresolved in these lines of work. It is noteworthy that recent developments such as [12] proposes moving the robot underneath the patient’s body, away from the beam. However, it is not yet certain that this would fully resolve the radiation attenuation issue. The human body given its soft tissues needs a manipulation system that cushions most of the energy arising

[†]Perelman School of Medicine, The University of Pennsylvania, Philadelphia, PA 19104, USA. ogunmolo@pennmedicine.upenn.edu

^{*}Department of Radiation Oncology, The University of Chicago, Chicago, IL 60637, USA. {xmliu, rwiersma}@uchicago.edu

[‡]Automation & Intelligent Systems Division, The University of Texas at Arlington Research Institute, Arlington, TX, USA. nick.gans@uta.edu

The research reported in this publication was supported by National Cancer Institute of the National Institutes of Health under award number R01CA227124.

out of collisions.

This is why we have proposed inflatable air bladders (IABs) as motion compensators during F&M RT treatment (see [13]–[16]). Our IABs are continuum, compliant, and configurable (C3) soft robot (SoRo) actuators, providing therapeutic patient motion compensation during RT. These actuators inflate, deflate, expand or contract based on their material moduli, internal pressurization and incompressibility constraints when given a reference trajectory. To our knowledge, ours are the first to explore C3 materials as actuation systems for cranial manipulation in robotic radiotherapy.

Contributions:

- We propose a motion correction mechanism that largely avoids dose attenuation, whilst providing patient comfort during motion correction in F&M cancer RT;
- For the proposed mechanism, we construct a constitutive model for the constituent C3 IABs by extending the principles of nonlinear elastic deformations [17], [18] to isochoric strain deformations of the IAB semi-rigid bodies;
- We then analyze their deformation under stress, strain, internal pressurization, and an arbitrary hydrostatic pressure.

This kinematic model will then be used to develop the kinematics and Lagrangian equations of the dynamics of the multi-dof motion correction mechanism. Particularly, we analyze the deformation of a single semi-rigid robot body. The rest of this paper is structured as follows: in § II, we present the overall C3 kinematic mechanism; we analyze the deformation properties of the IAB in § III; we then provide and discuss simulation results in § IV. We conclude the paper in § V.

II. MECHANISM DESCRIPTION

In our previous F&M RT IAB control investigation [15], we relied on a system identification approach to realize the overall system model. Our resultant model lumped the patient, treatment couch, as well as IAB models into one. The disadvantage of this approach was that such overall model lacked enough fidelity such that it necessitated the memory-based adaptive control composite laws that was derived from inverse Lyapunov analysis. Furthermore, the approximation model component of the ensuing neural-network controller required extensive training to realize a suitable controller for our H&N immobilization. Our goal here is to realize constitutive models for the IAB chains – capable of manipulating the patient’s H&N’s complete DOF motion in real-time during RT. This would enable us write closed-form expressions for the IAB chains’ complete kinematics.

A. Mechanism Setup

We now describe the mechanism of the complete motion compensation system. We propose 3 IAB kinematic chains totaling 8 IABs around the patient’s H&N region as illustrated in Fig. 3. The IABs are made out of silicone or rubber materials with a Poisson ration of approximately 0.5. They have an internal cavity surrounded by two shells, which are made out of incompressible materials. The internal cavity ensures the hollow IAB holds the head in place. The outer shell encapsulates the

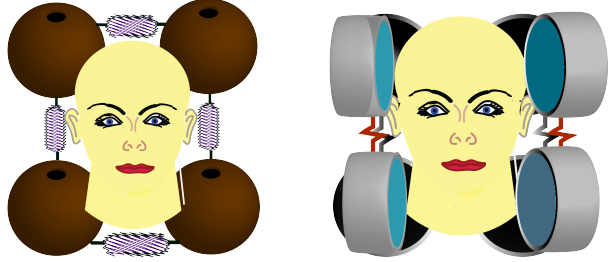


Fig. 2: An abstraction of the patient’s position correction mechanism. In the left image, there are four IABs that constitute the base kinematic chain. They lift the head along the Z-axis (up or down on the treatment table) as well as provide pitch motion corrections. On the right, the side kinematic chains provide roll and yaw motion corrections. [Image best visualized in colored print].

inner shell such that local volume preservation is fulfilled between configuration changes. This isochoric property and the incompressibility constraints of the IAB material is important in the mathematical derivations of the mechanism’s constitutive model.

There are two IAB chains to each side of the patient’s cranial region, each consisting of two IABs, linked by passive extensible connectors to accommodate head contact throughout manipulation – an important property for our contact kinematics. Each IAB makes contact with the forehead and the chin/neck region at either symmetry of the patient’s head. Underneath the patient’s H&N regions is a third closed kinematic chain. This chain consists of four IABs, each positioned at four cardinal contact points beneath the patient’s H&N region (see Fig. 2, and Fig. 3). The wearable mask of Fig. 4 is configurable to hold the chains in place around the patient’s H&N region. The IABs change their configuration based on air that flows into or out of their air chambers when the sensed deviation of the patient from a target exceeds a pose setpoint or a desired trajectory path. The degrees of freedom of the mechanism can be determined using *Gruëbler-Kutzbach’s mobility condition*, wherein the number of degrees of freedom of the mechanism is given by (when the actuation results in a non-planar workspace configuration)

$$F = 6(N - g) + \sum_{i=1}^g f_i \quad (1)$$

where N is the number of links in the mechanism, g is the number of joints, f_i is the total number of degrees of freedom for the i th joint. where through equations (1), the mechanism of has 16 DOFs given its $N = 8$ links, $g = 8$ joints, and each IAB joint is constrained along 2 DOFs .

B. Finite Elastic Deformation Model

We propose a finite elastic deformation model [17], [18], [20], based on the deformation invariants of the stored energy function of each IAB. In what follows, we briefly describe our motivation for devising a finite elastic deformation model. The constant curvature approach for parameterizing the deformation



Fig. 3: System setup in the SOFA Framework Architecture. **Top:** Gantry, Turntable, Patient and IAB Chains around the patient’s H&N Region. **Bottom:** Close-up view of compensating IABs around patient’s H&N region with the patient lying in a supine position on the treatment couch. [Image best visualized in colored print].

of continuum robots [21]–[23] has played significant role in the kinematic synthesis of deformable continuum models over the past three decades. Under this framework, the configuration space of a SoRo module is parameterized by the curvature of an arc projected on the SoRo’s body, the arc’s length, and the angle subtended by a tangent along that arc. The relationship between these parameters are typically found using differential kinematics with a Frenet-Serret frame that models a curve on the SoRo’s surface with or without torsion.

By abstracting an infinite dimensional structure to 3D, large portions of the manipulator dynamics are discarded under the assumption that the actuator design is symmetric and uniform in shape. This makes the constant curvature model overly simplistic so that it often exhibits poor performance in position control [24]. While the Cosserat brothers’ beam theory has been relatively successful in modeling soft continuum dynamics [25], [26], its complexity, and sensing cost does not justify the alternatives [27].

III. DEFORMATION ANALYSIS OF AN IAB

In this section, we present the deformation analysis of an IAB within the proposed mechanism: we address the invariants of deformation, and strain deformation. We then analyze the stress laws and constitutive relations that govern the IAB’s

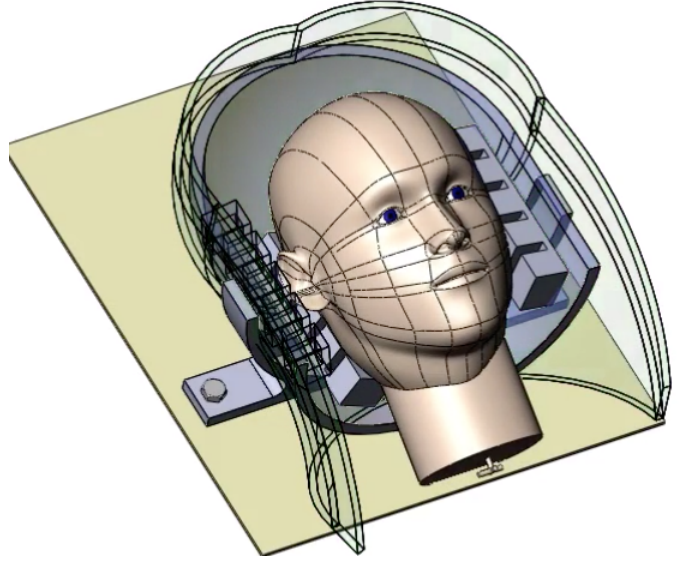


Fig. 4: Radio transparent reconfigurable semi-plastic mask model that holds the IABs in place around the patient’s H&N region. This follows our design in [19]. Unlike frame-based immobilization systems, the head can undergo complete motion manipulation inside the re-configurable wearable mask. [Image best visualized in colored print.]

deformation; we conclude the section by solving the boundary value problem under the assumptions of *isochoricity* and *incompressibility* of the IAB material skins. We present the kinematics of the IAB based on a relationship between internal pressure, Cauchy stress, stored strain energy, and the radii of the IAB. The IABs are made out of rubber components which have the distinct property of incompressibility with a Poisson ratio of approximately 0.5 [28]. Our overarching assumption is that volume does not change locally during deformation at a configuration $\chi(t)$ at time t . Since we consider only final configurations of the soft robot, we drop the explicit dependence of a configuration on time and write it as χ . We refer readers to background reading materials in [17], [29] and [28].

A. Deformation Invariants

For an elastic and incompressible IAB under the action of applied forces, the deformation is governed by a stored energy function, W , which captures the physical properties of the material [30]. We choose two invariants namely, I_1 , and I_2 , described in terms of the principal extension ratios, $\lambda_r, \lambda_\phi, \lambda_\theta$, of the IAB’s strain ellipsoids. They are defined as,

$$I_1 = \lambda_r^2 + \lambda_\phi^2 + \lambda_\theta^2, \quad \text{and} \quad I_2 = \lambda_r^{-2} + \lambda_\phi^{-2} + \lambda_\theta^{-2}. \quad (2)$$

Under the incompressibility assumptions of the IAB material, it follows that $\lambda_r \lambda_\phi \lambda_\theta = 1$ [18]. In spherical coordinates, the change in polar/azimuth angles as well as radii from the reference to current configurations are as illustrated in Fig. 5. Forces that produce deformations are derived using the strain energy-invariants relationship, *i.e.*, $\frac{\partial W}{\partial I_1}$ and $\frac{\partial W}{\partial I_2}$.

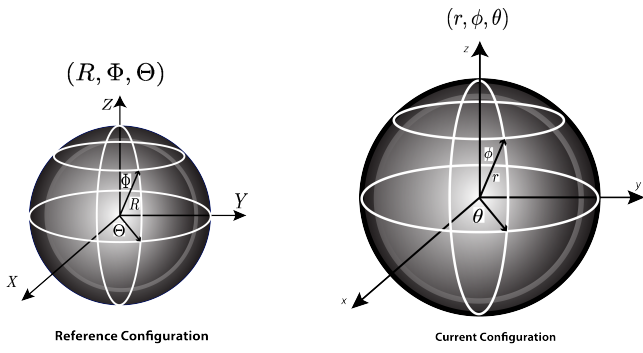


Fig. 5: Deformation in spherical polar coordinates.

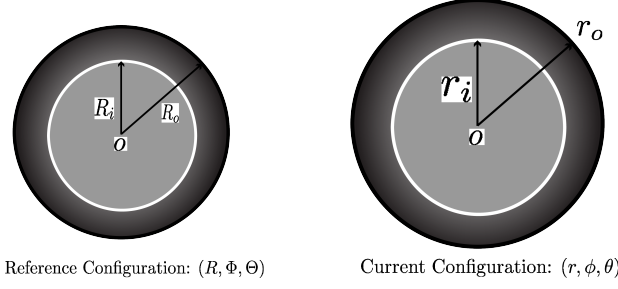


Fig. 6: Radii change under deformation.

B. Analysis of Strain Deformations

Suppose a particle on the IAB material surface in the reference configuration has coordinates (R, Φ, Θ) defined in spherical polar coordinates (see Fig. 5), where R represents the radial distance of the particle from a fixed origin, Θ is the azimuth angle on a reference plane through the origin and orthogonal to the polar angle, Φ . Denote the internal and external radii as R_i , and R_o respectively. We define the following constraints,

$$R_i \leq R \leq R_o, \quad 0 \leq \Theta \leq 2\pi, \quad 0 \leq \Phi \leq \pi. \quad (3)$$

Now, suppose that the IAB undergoes deformation under the application of pressure on the internal IAB walls as depicted in Fig. 6. Arbitrary points A and A' in the reference configuration become Q and Q' in the current configuration. Suppose that the vector that describes the *fiber* that connects points A and A' is $a = a_R e_r + a_\Theta e_\Theta + a_\Phi e_\Phi$ where e_r , e_Θ , and e_Φ are respectively the basis vectors for polar directions R , Θ , and Φ such that its axial length stretches *uniformly* by an amount $\lambda_z = \frac{r}{R}$. We assume that there are internal constraints such that spherical symmetry is maintained during deformation of the incompressible IAB material shell so that we have the following constraints in the current configuration

$$r_i \leq r \leq r_o, \quad 0 \leq \theta \leq 2\pi, \quad 0 \leq \phi \leq \pi. \quad (4)$$

The radial vectors \mathbf{R} and \mathbf{r} are given in spherical coordinates as,

$$\mathbf{R} = \begin{bmatrix} R \cos \Theta \sin \Phi, \\ R \sin \Theta \sin \Phi, \\ R \cos \Phi \end{bmatrix} \quad \text{and} \quad \mathbf{r} = \begin{bmatrix} r \cos \theta \sin \phi, \\ r \sin \theta \sin \phi, \\ r \cos \phi \end{bmatrix}. \quad (5)$$

The material volume $\frac{4}{3}\pi(R^3 - R_i^3)$ contained between spherical shells of radii R and R_i remains constant throughout

deformation, being equal in volume to $\frac{4}{3}\pi(r^3 - r_i^3)$ so that

$$\frac{4}{3}\pi(R^3 - R_i^3) = \frac{4}{3}\pi(r^3 - r_i^3) \quad r^3 = R^3 + r_i^3 - R_i^3. \quad (6)$$

The homogeneous deformation between the two configurations imply that

$$r^3 = R^3 + r_i^3 - R_i^3, \quad \theta = \Theta, \quad \phi = \Phi, \quad (7)$$

where the coordinates obey the constraints of equations (3) and (4). The Mooney-Rivlin strain energy for small deformations as a function of the strain invariants of (2), is,

$$W' = C_1(I_1 - 3) + C_2(I_2 - 3), \quad (8)$$

where C_1 and C_2 are appropriate choices for the IAB material moduli. The Mooney form (8) has been shown to be valid even for large elastic deformations, provided that the elastic materials exhibit incompressibility and are isotropic in their reference configurations [20]. For mathematical scaling purposes that will soon become apparent, we rewrite (8) as $W = \frac{1}{2}W'$ so that

$$W = \frac{1}{2}C_1(I_1 - 3) + \frac{1}{2}C_2(I_2 - 3). \quad (9)$$

Note that equation (8) or (9) becomes the neo-Hookean strain energy relation when $C_2 = 0$. The gradient tensor operator in spherical-polar coordinates is,

$$\begin{aligned} \mathbf{F} &= \lambda_r \mathbf{e}_r \otimes \mathbf{e}_R + \lambda_\phi \mathbf{e}_\phi \otimes \mathbf{e}_\Phi + \lambda_\theta \mathbf{e}_\theta \otimes \mathbf{e}_\Theta \\ &= \frac{R^2}{r^2} \mathbf{e}_r \otimes \mathbf{e}_R + \frac{r}{R} \mathbf{e}_\phi \otimes \mathbf{e}_\Phi + \frac{r}{R} \mathbf{e}_\theta \otimes \mathbf{e}_\Theta, \end{aligned} \quad (10)$$

where \otimes denotes the dyadic product [17]. It can be verified that the radial stretch is $\lambda_r = \frac{R^2}{r^2}$. The principal stretches along the azimuthal and zenith axes imply that $\lambda_\theta = \lambda_\phi$. Since for an isochoric deformation, $\lambda_r \cdot \lambda_\theta \cdot \lambda_\phi = 1$, the principal extension ratios are

$$\lambda_r = \frac{R^2}{r^2}; \quad \lambda_\theta = \lambda_\phi = \frac{r}{R}.$$

The invariant equations, in polar coordinates, are therefore a function of the right and left Cauchy-Green deformation tensors *i.e.*,

$$I_1 = \mathbf{tr}(\mathbf{C}) = \frac{R^4}{r^4} + \frac{2r^2}{R^2}, \quad I_2 = \mathbf{tr}(\mathbf{C}^{-1}) = \frac{r^4}{R^4} + \frac{2R^2}{r^2}, \quad (11)$$

where, $\mathbf{C} = \mathbf{F}^T \mathbf{F}$ and $\mathbf{B} = \mathbf{FF}^T$ are the right and left Cauchy-Green tensors.

C. Stress Laws and Constitutive Equations

We are concerned with the magnitudes of the differential stress on the IAB skin from a mechanical point of view. Since the IAB deforms at ambient temperature, we take thermodynamic properties such as temperature and entropy to have negligible contribution. The IAB material stress response, \mathbf{G} , at any point on the IAB's boundary at time t determines the Cauchy stress, σ , as well as the history of the motion up to and at the time t [17]. The constitutive relation for the nominal

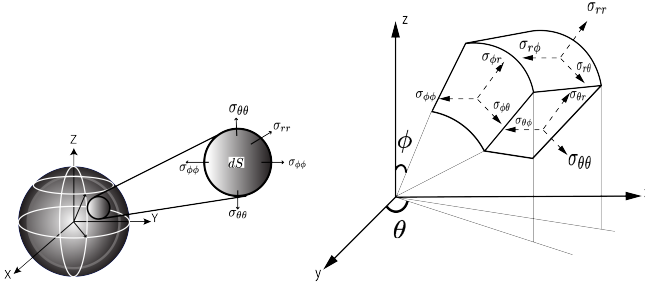


Fig. 7: Stress distribution on the IAB's differential surface, dS .

stress deformation for an elastic IAB material is given by

$$\boldsymbol{\sigma} = \mathbf{G}(\mathbf{F}) + q\mathbf{F}\frac{\partial \boldsymbol{\Lambda}}{\partial \mathbf{F}}(\mathbf{F}), \quad (12)$$

where \mathbf{G} is a functional with respect to the configuration χ_t , q acts as a Lagrange multiplier, and $\boldsymbol{\Lambda}$ denotes the internal (incompressibility) constraints of the IAB system. For an incompressible material, the indeterminate Lagrange multiplier becomes the hydrostatic pressure *i.e.* $q = -p$ [29]. The incompressibility of the IAB material properties imply that $\boldsymbol{\Lambda} \equiv \det \mathbf{F} - 1$. Evaluating the partial derivative of $\boldsymbol{\Lambda}(\mathbf{F})$ with respect to \mathbf{F} and substituting $-p$ for q in (12), we have

$$\begin{aligned} \boldsymbol{\sigma} &= \mathbf{G}(\mathbf{F}) - p\mathbf{F}\text{adj}^T(\mathbf{F}) \\ &= \mathbf{G}(\mathbf{F}) - p\mathbf{F}\mathbf{F}^{-T}\det(\mathbf{F}) \\ &= \mathbf{G}(\mathbf{F}) - p\mathbf{I}, \end{aligned} \quad (13)$$

where the last part of the equation follows from the isochoric assumption *i.e.*, $\det(\mathbf{F}) = 1$. In terms of the stored strain energy, we can rewrite (13) as

$$\boldsymbol{\sigma} = \begin{bmatrix} \sigma_{rr} & \sigma_{r\phi} & \sigma_{r\theta} \\ \sigma_{\phi r} & \sigma_{\phi\phi} & \sigma_{\phi\theta} \\ \sigma_{\theta r} & \sigma_{\theta\phi} & \sigma_{\theta\theta} \end{bmatrix} = \frac{\partial W}{\partial \mathbf{F}} \mathbf{F}^T - p\mathbf{I}, \quad (14)$$

where \mathbf{I} is the identity tensor and p represents an arbitrary hydrostatic pressure. A visualization of the component stresses of (14) on the outer shells of the IAB material is illustrated in Fig. 7. It follows that the constitutive law that governs the Cauchy stress tensor is

$$\begin{aligned} \boldsymbol{\sigma} &= \frac{\partial W}{\partial \mathbf{I}_1} \cdot \frac{\partial \mathbf{I}_1}{\partial \mathbf{F}} \mathbf{F}^T + \frac{\partial W}{\partial \mathbf{I}_2} \cdot \frac{\partial \mathbf{I}_2}{\partial \mathbf{F}} \mathbf{F}^T - p\mathbf{I} \\ &= \frac{1}{2}C_1 \frac{\partial \text{tr}(\mathbf{F}\mathbf{F}^T)}{\partial \mathbf{F}} \mathbf{F}^T + \frac{1}{2}C_2 \frac{\partial \text{tr}([\mathbf{F}^T \mathbf{F}]^{-1})}{\partial \mathbf{F}} \mathbf{F}^T - p\mathbf{I} \\ &= \frac{1}{2}C_1 (2\mathbf{F}\mathbf{F}^T) + \frac{1}{2}C_2 (-2\mathbf{F}(\mathbf{F}^T \mathbf{F})^{-2}) \mathbf{F}^T - p\mathbf{I} \\ &= C_1 \mathbf{F}\mathbf{F}^T - C_2 (\mathbf{F}^T \mathbf{F})^{-1} - p\mathbf{I} \\ \boldsymbol{\sigma} &= C_1 \mathbf{B} - C_2 \mathbf{C}^{-1} - p\mathbf{I}, \end{aligned} \quad (15)$$

from which we can write the normal stress components as

$$\sigma_{rr} = -p + C_1 \frac{R^4}{r^4} - C_2 \frac{r^4}{R^4} \quad (16a)$$

$$\sigma_{\theta\theta} = \sigma_{\phi\phi} = -p + C_1 \frac{r^2}{R^2} - C_2 \frac{R^2}{r^2}. \quad (16b)$$

D. IAB Boundary Value Problem

Here, we analyze the stress and internal pressure of the IAB at equilibrium. Consider the IAB with boundary conditions given by,

$$\sigma_{rr}|_{R=R_o} = -P_{\text{atm}}, \quad \sigma_{rr}|_{R=R_i} = -P_{\text{atm}} - P \quad (17)$$

where P_{atm} is the atmospheric pressure and $P > 0$ is the internal pressure exerted on the walls of the IAB above P_{atm} *i.e.*, $P > P_{\text{atm}}$. Suppose that the IAB stress components satisfy hydrostatic equilibrium, the equilibrium equations for the body force \mathbf{b}' 's physical component vectors, b_r, b_θ, b_ϕ are

$$\begin{aligned} -b_r &= \frac{1}{r^2} \frac{\partial r^2 \sigma_{rr}}{\partial r} + \frac{1}{r \sin \phi} \frac{\partial \sin \phi \sigma_{r\phi}}{\partial \phi} + \frac{1}{r \sin \phi} \frac{\partial \sigma_{r\theta}}{\partial \theta} \\ &\quad - \frac{1}{r} (\sigma_{\theta\theta} + \sigma_{\phi\phi}) \end{aligned} \quad (18a)$$

$$\begin{aligned} -b_\phi &= \frac{1}{r^3} \frac{\partial r^3 \sigma_{r\phi}}{\partial r} + \frac{1}{r \sin \phi} \frac{\partial \sin \phi \sigma_{\phi\phi}}{\partial \phi} + \frac{1}{r \sin \phi} \frac{\partial \sigma_{\phi\theta}}{\partial \theta} \\ &\quad - \frac{\cot \phi}{r} (\sigma_{\theta\theta}) \end{aligned} \quad (18b)$$

$$-b_\theta = \frac{1}{r^3} \frac{\partial r^3 \sigma_{\theta r}}{\partial r} + \frac{1}{r \sin^2 \phi} \frac{\partial \sin^2 \phi \sigma_{\theta\phi}}{\partial \phi} + \frac{1}{r \sin \phi} \frac{\partial \sigma_{\theta\theta}}{\partial \theta} \quad (18c)$$

(see [31]). From the equation of balance of linear momentum (*Cauchy's first law of motion*), we have that

$$\text{div } \boldsymbol{\sigma}^T + \rho \mathbf{b} = \rho \dot{\mathbf{v}} \quad (19)$$

where ρ is the IAB body mass density, div is the divergence operator, and $\mathbf{v}(\mathbf{x}, t) = \dot{\chi}_t(\mathbf{X})$ is the velocity gradient. Owing to the incompressibility assumption, we remark in passing that the mass density is uniform throughout the body of the IAB material. When the IAB is at rest, $\dot{\mathbf{v}}_t(\mathbf{x}) = 0 \forall \mathbf{x} \in \mathcal{B}$ such that equation (19) loses its dependence on time. The assumed regularity of the IAB in the reference configuration thus leads to the steady state conditions for Cauchy's first equation; the stress field $\boldsymbol{\sigma}$ becomes *self-equilibrated* by virtue of the spatial divergence and the symmetric properties of the stress tensor, so that we have

$$\text{div } \boldsymbol{\sigma} = 0. \quad (20)$$

Equation 20 is satisfied if the hydrostatic pressure p in (15) is independent of θ and ϕ . Therefore, we are left with (18a) so that we have

$$\frac{1}{r} \frac{\partial}{\partial r} (r^2 \sigma_{rr}) = (\sigma_{\theta\theta} + \sigma_{\phi\phi}). \quad (21)$$

Expanding, we find that

$$\frac{1}{r} \left[r^2 \frac{\partial \sigma_{rr}}{\partial r} + \sigma_{rr} \frac{\partial (r^2)}{\partial r} \right] = (\sigma_{\theta\theta} + \sigma_{\phi\phi}) \quad (22)$$

$$r \frac{\partial \sigma_{rr}}{\partial r} = \sigma_{\theta\theta} + \sigma_{\phi\phi} - 2\sigma_{rr} \quad (23)$$

$$\frac{\partial \sigma_{rr}}{\partial r} = \frac{1}{r} (\sigma_{\theta\theta} + \sigma_{\phi\phi} - 2\sigma_{rr}). \quad (24)$$

Integrating the above equation in the variable r , and taking $\sigma_{rr}(r_o) = 0$, we find that

$$\begin{aligned}\sigma_{rr}(r) &= - \int_{r_i}^{r_o} \frac{1}{r} (\sigma_{\theta\theta} + \sigma_{\phi\phi} - 2\sigma_{rr}) dr, \\ &= - \int_{r_i}^{r_o} \left[2C_1 \left(\frac{r}{R^2} - \frac{R^4}{r^5} \right) + 2C_2 \left(\frac{r^3}{R^4} - \frac{R^2}{r^3} \right) \right] dr.\end{aligned}\quad (24)$$

The above relation gives the radial stress in the current configuration. Suppose we are in the current configuration and we desire to revert to the reference configuration, we may carry out a change of variables from r to R as follows,

$$\begin{aligned}\sigma_{rr}(R) &= - \int_{R_i}^{R_o} \frac{1}{r} (\sigma_{\theta\theta} + \sigma_{\phi\phi} - 2\sigma_{rr}) \frac{dr}{dR} dR, \\ &= - \int_{R_i}^{R_o} \left[2C_1 \left(\frac{1}{r} - \frac{R^6}{r^7} \right) - 2C_2 \left(\frac{R^4}{r^5} - \frac{r}{R^2} \right) \right] dR.\end{aligned}\quad (25)$$

In the same vein, using the boundary condition of (17)|₂ and taking the ambient pressure $P_{\text{atm}} = 0$, we find that the internal pressure $P = -\sigma_{rr}(r) = -\sigma_{rr}(R)$ i.e.

$$\begin{aligned}P(r) &= \int_{r_i}^{r_o} \left[2C_1 \left(\frac{r}{R^2} - \frac{R^4}{r^5} \right) + 2C_2 \left(\frac{r^3}{R^4} - \frac{R^2}{r^3} \right) \right] dr \\ P(R) &\equiv \int_{R_i}^{R_o} \left[2C_1 \left(\frac{1}{r} - \frac{R^6}{r^7} \right) - 2C_2 \left(\frac{R^4}{r^5} - \frac{r}{R^2} \right) \right] dR.\end{aligned}\quad (26)$$

Equations (25) and (26) completely determine the deformation kinematics of the IAB material. Under the incompressibility of the IAB material properties we have,

$$r^3 = R^3 + r_i^3 - R_i^3, \text{ and } r_o^3 = R_o^3 + r_i^3 - R_i^3. \quad (27)$$

IV. SIMULATION

We conduct simulations under volumetric deformation with different shell properties (stated in the tables of Figs 8-11). We fix both reference configuration radii and choose physically realistic volumetric moduli for the IAB shells. By specifying a desired radially symmetric expansion for the inner IAB material, we test the local volume preservation property of (6) and evaluate the resulting displacement of the outer IAB skin, by applying the computed pressure (by virtue of (26)) to the IAB between configurations. The computed soft mesh model of the IAB is shown in the top middle of the charts while the stress distribution after the application of the calculated pressure is shown in the upper-right corner of the figures. We chose a Poisson ratio of 0.45 – 0.5 to model the IAB incompressibility properties. The radii dimensions are in cm, the pressure is given in psi unless otherwise stated, C_1 and C_2 are appropriate material moduli, and ΔV is the volumetric change between the IAB shells between configurations (given in cm^3).

A. Results: Volumetric Expansion

In Fig. 8 we test finite elastic deformation of the IAB material shells. We fix the internal and external radii in the reference configuration as 10cm and 15cm respectively. Our goal was to

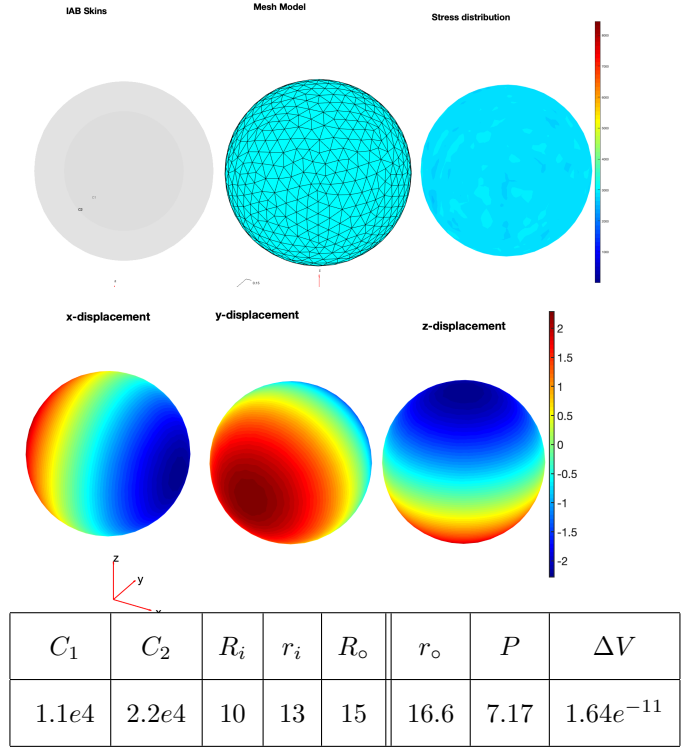


Fig. 8: IAB Expansion I [Best visualized in colored print].

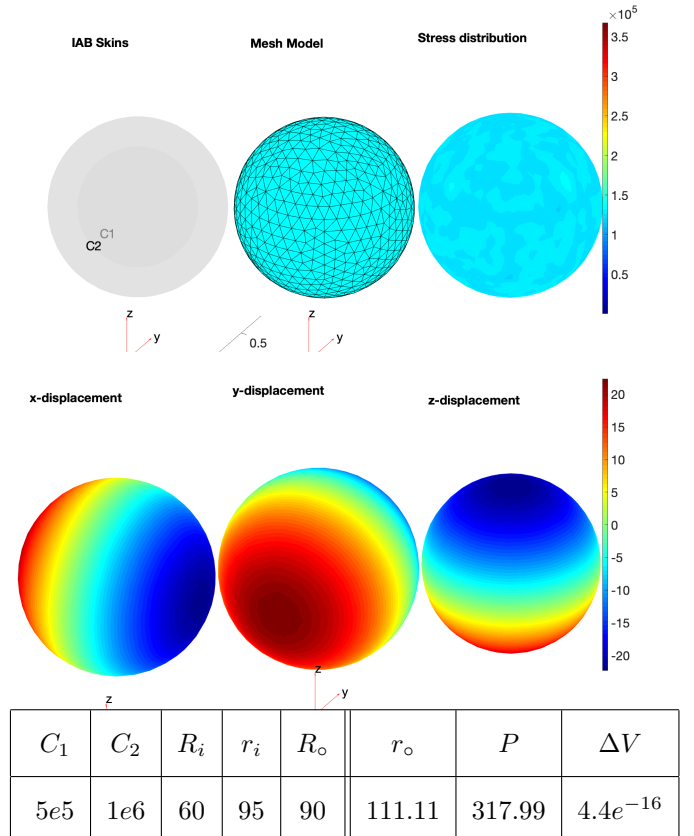


Fig. 9: IAB Expansion II [Best visualized in colored print].

radially expand the internal shell by a 3cm. By (7), we found r_o to be 111.11cm, meaning applying the calculated pressure using relation (26) should ideally generate a 1.6cm uniform

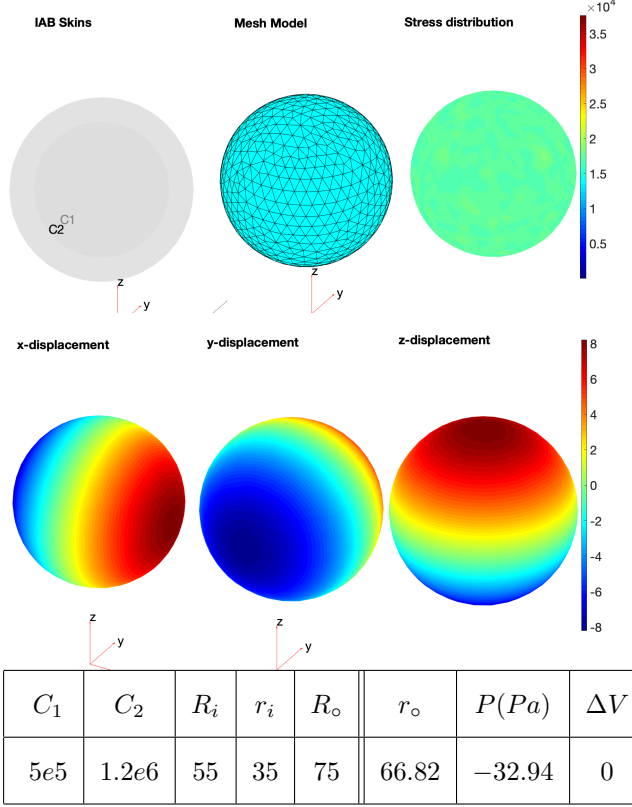


Fig. 10: IAB Compression I [Best visualized in colored print].

displacement on the outer IAB shell. Notice the uniform displacement of $1.6\text{cm} \pm 0.1\text{cm}$ along the Cartesian coordinates of the lower charts of the figure.

Following the convention that finite elastic deformations are valid for fairly large deformations [18], [20], [30], we tested the proposed constitutive laws in the expansion case of Fig. 9: given $R_i = 60\text{cm}$, $R_o = 90\text{cm}$ in the reference configuration, we would like to find the pressure that deforms the IAB so that $r_i = 95\text{cm}$. Again, we find $r_o = 111.11\text{cm}$ by (7). Applying the calculated pressure, we find the IAB displacement between configurations (lower portion of Fig. 8) to be $\approx 21.11\text{cm}$. We observe local volume preservation between the shells with volume between the shells essentially unchanged ($\equiv \Delta V$) in the table.

B. Results: Volumetric Compression

The deformation cases of Figures 10 and 11 depict the volumetric compression of the incompressible IAB under the application of the derived internal pressure for a desired radial shrink. The negative pressure in the tables signify that air is flowing out of the bladders. Again, we notice a uniform stress distribution on the IAB shells.

In Fig. 10, for a desired uniform displacement 8.18cm , our results confirm the validity of the stress-strain constitutive laws, as we notice a displacement of $\approx 8.2\text{cm}$ along the sphere's Cartesian axes in the lower charts of the figure. Similar to the expansion cases earlier described, we carry out a second experiment for finite elastic deformation for minute displacements of the IAB shells (Fig. 11). Again, our results show consistency with respect to volume preservation and

radially symmetric displacement.

C. Discussion

Notice a uniform stress distribution on the IAB walls in all test cases. We also notice that despite the internal and external radii change from between configurations, the volume is preserved within the IAB shells according to (6). This confirms our leading hypothesis. Because the isochoric assumption is a good first-order approximation for the incompressible IAB material behavior, it is natural to expect that the shells would dent when in contact with the head. Different patients have different cranial anatomical characteristics such that the amount of dent that would be caused by a patient cannot be accurately predicted without extensive statistical analysis before treatment. And if at all this is baked into our model, the constituent spherical harmonics model for the dents would only complicate the overall model – increasing kinematic solve time. To avoid this, we have chosen stronger material moduli for the outer IAB shell (as seen in the tables). This simplifies the IAB kinematics during contact while preserving the continuum properties just derived.

V. CONCLUSIONS

We have presented the IAB motion-correction mechanism for frameless and maskless RT as well as the constitutive laws that govern the deformation of the mechanism's constituent IABs. Our results confirm our constitutive relations, satisfying the local volume preservation principle. The key hardware design to avoiding a complicated mathematical model is to choose the elastic modulus of the IAB skins such that in equilibrium,

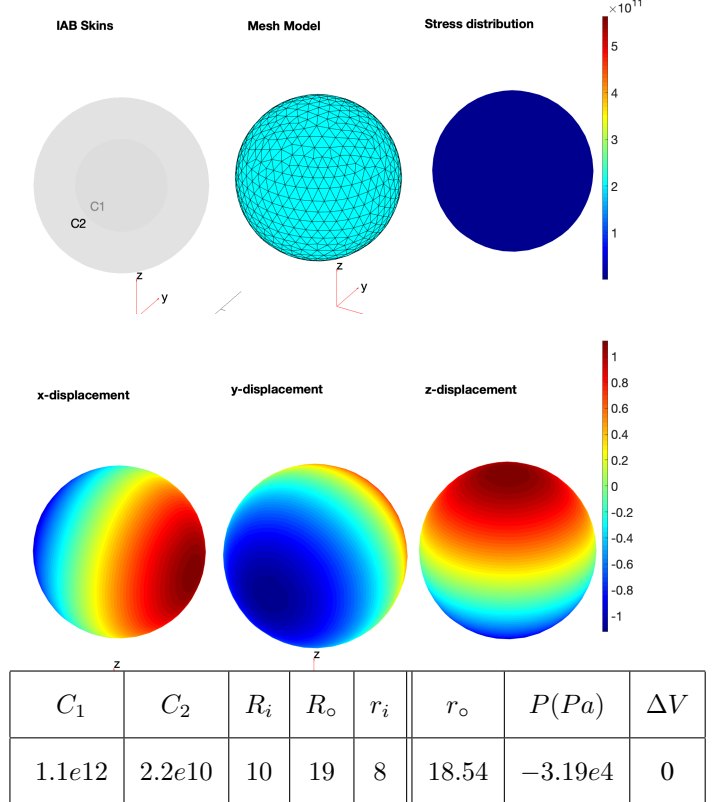


Fig. 11: IAB Compression II [Best visualized in colored print].

during, or between configuration transformations, the IAB material mostly holds the (isochoric) bulk compression and expansion property. To prevent puncture and damage arising from intermittent pneumatic pressurization of the walls of the IAB, we could consider the presence of glass fibers, carbon nanotubes to the elastomeric matrix as proposed in [32]. We have left out such considerations until such time after we would have validated the deformation property of the IAB model presented herein on a hardware in the real-time positioning of the patient in F&M RT. In a future work, we will analyze the IABs' contact dynamics with the patient's cranial region and then construct the kinematics and dynamics model for the H&N control in real-time RT.

VI. ACKNOWLEDGMENTS

A vote of thanks to Audrey Sedal of The University of Michigan for her feedback on the presented constitutive model.

REFERENCES

- [1] L. Gaspar *et al.*, ‘‘Recursive Partitioning Analysis (rpa) of Prognostic Factors in three Radiation Therapy Oncology Group (rtog) Brain Metastases Trials,’’ *Int. J. Radiat. Oncol. Biol. Phys.*, vol. 37, p. 745–751, 1997. [1](#)
- [2] T. Takakura, T. Mizowaki, M. Nakata, S. Yano, T. Fujimoto, Y. Miyabe, M. Nakamura, and M. Hiraoka, ‘‘The geometric accuracy of frameless stereotactic radiosurgery using a 6d robotic couch system,’’ *Physics in Medicine & Biology*, vol. 55, no. 1, p. 1, 2009. [1](#)
- [3] L. I. Cerviño, N. Detorie, M. Taylor, J. D. Lawson, T. Harry, K. T. Murphy, A. J. Mundt, S. B. Jiang, and T. A. Pawlicki, ‘‘Initial Clinical Experience with a Frameless and Maskless Stereotactic Radiosurgery Treatment,’’ *Practical Radiation Oncology*, vol. 2, no. 1, pp. 54–62, 2012. [1](#)
- [4] L. I. Cerviño, T. Pawlicki, J. D. Lawson, and S. B. Jiang, ‘‘Frame-less and mask-less cranial stereotactic radiosurgery: a feasibility study,’’ *Physics in medicine and biology*, vol. 55, no. 7, p. 1863, 2010. [1](#)
- [5] M. J. Murphy, R. Eidens, E. Vertatschitsch, and J. N. Wright, ‘‘The effect of transponder motion on the accuracy of the calypso electromagnetic localization system,’’ *International Journal of Radiation Oncology* Biology* Physics*, vol. 72, no. 1, pp. 295–299, 2008. [1](#)
- [6] A. Navarro-Martin, J. Cacicedo, O. Leaman, I. Sancho, E. García, V. Navarro, and F. Guedea, ‘‘Comparative analysis of thermoplastic masks versus vacuum cushions in stereotactic body radiotherapy,’’ *Radiation Oncology*, vol. 10, no. 1, p. 176, 2015. [1](#)
- [7] G. Li, A. Ballangrud, M. Chan, R. Ma, K. Beal, Y. Yamada, T. Chan, J. Lee, P. Parhar, J. Mechala *et al.*, ‘‘Clinical Experience with two Frameless Stereotactic Radiosurgery (fsrs) Systems using Optical Surface Imaging for Motion Monitoring,’’ *Journal of Applied Clinical Medical Physics/American College of Medical Physics*, vol. 16, no. 4, p. 5416, 2015. [1](#)
- [8] A. Krauss, S. Nill, M. Tacke, and U. Oelfke, ‘‘Electromagnetic real-time tumor position monitoring and dynamic multileaf collimator tracking using a siemens 160 mlc: Geometric and dosimetric accuracy of an integrated system,’’ *International Journal of Radiation Oncology* Biology* Physics*, vol. 79, no. 2, pp. 579–587, 2011. [1](#)
- [9] X. Liu, A. H. Belcher, Z. Grelewicz, and R. D. Wiersma, ‘‘Robotic stage for head motion correction in stereotactic radiosurgery,’’ in *2015 American Control Conference (ACC)*. IEEE, 2015, pp. 5776–5781. [1](#)
- [10] C. Herrmann, L. Ma, and K. Schilling, ‘‘Model Predictive Control For Tumor Motion Compensation In Robot Assisted Radiotherapy,’’ *IFAC Proceedings Volumes*, vol. 44, no. 1, pp. 5968–5973, 2011. [1](#)
- [11] A. Belcher, ‘‘Patient Motion Management with 6-DOF Robotics for Frameless and Maskless Stereotactic Radiosurgery,’’ Ph.D. dissertation, The University of Chicago, 2017. [1](#)
- [12] X. Liu and R. D. Wiersma, ‘‘Optimization based trajectory planning for real-time 6DoF robotic patient motion compensation systems,’’ *PloS one*, vol. 14, no. 1, p. e0210385, 2019. [1](#)
- [13] O. P. Ogunmolu, X. Gu, S. Jiang, and N. R. Gans, ‘‘A real-time, soft robotic patient positioning system for maskless head-and-neck cancer radiotherapy: An initial investigation,’’ in *Automation Science and Engineering (CASE), 2015 IEEE International Conference on, Gothenburg, Sweden*. IEEE, 2015, pp. 1539–1545. [2](#)
- [14] O. P. Ogunmolu, X. Gu, S. Jiang, and N. R. Gans, ‘‘Vision-based control of a soft robot for maskless head and neck cancer radiotherapy,’’ in *Automation Science and Engineering (CASE), 2016 IEEE International Conference on, Fort Worth, Texas*. IEEE, 2016, pp. 180–187. [2](#)
- [15] O. Ogunmolu, A. Kulkarni, Y. Tadesse, X. Gu, S. Jiang, and N. Gans, ‘‘Soft-neuroadapt: A 3-dof neuro-adaptive patient pose correction system for frameless and maskless cancer radiotherapy,’’ in *IEEE/RSJ International Conference on Intelligent Robots and Systems (IROS), Vancouver, BC, CA*. IEEE, 2017, pp. 3661–3668. [2](#)
- [16] O. P. Ogunmolu, ‘‘A Multi-DOF Soft Robot Mechanism for Patient Motion Correction and Beam Orientation Selection in Cancer Radiation Therapy.’’ Ph.D. dissertation, The University of Texas at Dallas, 2019. [2](#)
- [17] R. Ogden, *Non-linear Elastic Deformations*. Mineola, New York: Dover Publications, Inc., 1997. [2, 3, 4](#)
- [18] L. R. G. Treloar, *The physics of rubber elasticity*. Oxford University Press, USA, 1975. [2, 3, 7](#)
- [19] Y. Almubarak, A. Joshi, O. Ogunmolu, X. Gu, S. Jiang, N. Gans, and Y. Tadesse, ‘‘Design and development of soft robot for head and neck cancer radiotherapy,’’ in *Electroactive Polymer Actuators and Devices (EAPAD) XX*, vol. 10594. International Society for Optics and Photonics, 2018, p. 1059418. [3](#)
- [20] M. Mooney, ‘‘A theory of large elastic deformation,’’ *Journal of applied physics*, vol. 11, no. 9, pp. 582–592, 1940. [2, 4, 7](#)
- [21] M. W. Hannan and I. D. Walker, ‘‘Kinematics and the Implementation of an Elephant’s Trunk Manipulator and Other Continuum Style Robots,’’ *Journal of Robotic Systems*, vol. 20, no. 2, pp. 45–63, 2003. [3](#)
- [22] M. W. Hannan and I. D. Walker, ‘‘Novel Kinematics for Continuum Robots.’’ *Advances in Robot Kinematics*, 2000, pp. 227–238. [3](#)
- [23] B. A. Jones and I. D. Walker, ‘‘Kinematics for Multisection Continuum Robots.pdf,’’ vol. 22, no. 1, pp. 43–55, 2006. [3](#)
- [24] A. D. Kapadia, K. E. Fry, and I. D. Walker, ‘‘Empirical investigation of closed-loop control of extensible continuum manipulators,’’ in *2014 IEEE/RSJ International Conference on Intelligent Robots and Systems*. IEEE, 2014, pp. 329–335. [3](#)
- [25] F. Renda, M. Giorelli, M. Calisti, M. Cianchetti, and C. Laschi, ‘‘Dynamic model of a multibending soft robot arm driven by cables,’’ *IEEE Transactions on Robotics*, vol. 30, no. 5, pp. 1109–1122, 2014. [3](#)
- [26] D. Trivedi, A. Lotfi, and C. D. Rahn, ‘‘Geometrically Exact Models For Soft Robotic Manipulators,’’ *IEEE Transactions on Robotics*, vol. 24, no. 4, pp. 773–780, 2008. [3](#)
- [27] T. George Thuruthel, Y. Ansari, E. Falotico, and C. Laschi, ‘‘Control Strategies for Soft Robotic Manipulators: A Survey,’’ *Soft Robotics*, vol. 5, no. 2, pp. 149–163, 2018. [3](#)
- [28] A. Gent, *Engineering with Rubber: How to Design Rubber Components*. Munich: Carl Hanser Verlag Publications, 2012. [3](#)
- [29] G. A. Holzapfel, T. C. Gasser, and R. W. Ogden, ‘‘A new constitutive framework for arterial wall mechanics and a comparative study of material models,’’ *Journal of elasticity and the physical science of solids*, vol. 61, no. 1-3, pp. 1–48, 2000. [3, 5](#)
- [30] R. S. Rivlin and D. W. Saunders, ‘‘Large Elastic Deformations of Isotropic Materials. VII. Experiments on the Deformation of Rubber,’’ *Philosophical Transactions of the Royal Society A: Mathematical, Physical and Engineering Sciences*, vol. 243, no. 865, pp. 251–288, 1950. [3, 7](#)
- [31] Y. Fung, P. Tong, and X. Chen, *Classical and computational solid mechanics*. World Scientific Publishing Company, 2001, vol. 2. [5](#)
- [32] R. F. Shepherd, A. A. Stokes, R. M. Nunes, and G. M. Whitesides, ‘‘Soft machines that are resistant to puncture and that self seal,’’ *Advanced Materials*, vol. 25, no. 46, pp. 6709–6713, 2013. [8](#)